48th AIAA Aerospace Sciences Meeting Including the New Horizons Forum and Aerospace Exposition
4 - 7 January 2010, Orlando, Florida
AIAA 2010-447

Parameter Sensitivity Analysis for Hypersonic Viscous Flow using a Discrete Adjoint Approach

Brian A. Lockwood*and Dimitri J. Mavriplis†
Department of Mechanical Engineering, University of Wyoming, Laramie, Wyoming, 82071-3295

A discrete adjoint approach for calculating sensitivity derivatives in viscous hypersonic flows is examined. The approach is presented within the context of both perfect gas and nonequilibrium real gas simulations and can be used to determine the sensitivity of objectives to various model and design parameters. By using an adjoint based approach, the sensitivity of an objective to a large number of input parameters can be calculated in an efficient and timely manner. In order to demonstrate the feasibility of the adjoint approach, a two dimensional cell-centered finite volume solver is presented and several sensitivity derivatives are calculated using a perfect gas and a five species, two temperature real gas model. Geometric sensitivities are presented for both models as well as sensitivity to various model parameters.

I. Introduction

The simulation of hypersonic flows involves numerous constitutive relations, each of which has a number of experimentally derived constants and parameters. The effect of these model parameters on engineering quantities, such as surface heating, is of importance for design optimization and uncertainty quantification. In previous work, a Monte Carlo approach has been used to quantify uncertainty and determine the sensitivity of simulation objectives to input parameters. This approach samples input parameters according to a probability density function and uses thousands of flow solves to determine the effect of variations in input parameters on flow objectives,[1].[2] To reduce the amount of time required to determine sensitivity derivatives and to make feasible the determinant of uncertainties due to a wider range of model parameters, a discrete adjoint approach is proposed. First, a flow solution using the perfect gas assumption is presented and compared against those produced by existing solvers. In addition to perfect gas results, a real gas flow solution is shown and the results are compared against the LAURA code.[3] With the flow solver demonstrated, a discrete adjoint for a perfect gas solution is presented. Using this adjoint, the sensitivity of integrated surface heating to normal displacements of surface points is calculated, as well as the sensitivity of surface heating to the perfect gas model parameter γ. In addition to the perfect gas sensitivities, geometric sensitivities for a real gas solution are presented. Parameter sensitivity for the real gas model is also explored and demonstrated for parameters relating to reaction rates, energy relaxation and transport. Finally, the use of the flow adjoint to determine the sensitivity of an objective to field quantities throughout the domain is demonstrated.

II. Flow Problem

II.A. Physical Models

For this work, the Navier Stokes equations are solved numerically via a cell centered finite volume scheme on unstructured meshes using triangular and/or quadrilateral elements. In vector form, the Navier Stokes equations are given by:

$$\frac{\partial \mathbf{U}}{\partial t} + \nabla \cdot \vec{F}(\mathbf{U}) = \nabla \cdot \vec{F}_v(\mathbf{U}) + \mathbf{S}(\mathbf{U}) \tag{1}$$

*Graduate Student; email: blockwoo@uwyo.edu
†Professor, AIAA Associate Fellow; email: mavripl@uwyo.edu

The variable $\mathbf{U}$ contains the conserved variables. The vectors $\vec{F}$ and $\vec{F}_v$ represent the inviscid and viscous fluxes, respectively. The vector $\mathbf{S}$ contains any source terms for the equations. In general, these source terms may be functions of the conserved variables. The exact terms in these equations depend on the physical model adopted for the analysis problem.

For a perfect gas, the conserved variables and flux vectors are given by:

$$\mathbf{U} = \left\{ \begin{array}{c} \rho \\ \rho\vec{u} \\ \rho e_t \end{array} \right\} \quad \vec{F} = \left\{ \begin{array}{c} \rho\vec{u} \\ \rho\vec{u} \otimes \vec{u} + P \\ \rho\vec{u}h_t \end{array} \right\} \quad \vec{F}_v = \left\{ \begin{array}{c} 0 \\ \underline{\tau} \\ \underline{\tau} \cdot \vec{u} - \vec{q} \end{array} \right\}$$

The shear stress tensor, $\underline{\tau}$, is given by the relation for a Newtonian fluid and the heat flux is represented by Fourier's law of conduction. Furthermore, the system is closed by invoking the thermal equation of state for a perfect gas. These relations are summarized below.

$$\underline{\tau} = \mu(\nabla\vec{u} + \vec{u}\nabla) - \frac{2}{3}\mu\nabla \cdot \vec{u}\underline{I} \tag{2}$$

$$\vec{q} = -k\nabla T \tag{3}$$

$$P = (\gamma - 1)\left[\rho e_t - \rho\frac{\vec{u} \cdot \vec{u}}{2}\right] \tag{4}$$

For a perfect gas, the source vector is zero in the absence of body forces. The variable γ in the above relation is constant by definition for a perfect gas. The variables μ and k are typically determined by empirical relationships. For this work, Sutherland's Law is used to model μ as a function of temperature and thermal conductivity is determined by assuming a constant Prandtl number. The perfect gas model has relatively few parameters which define its constitutive relations. These parameters are γ, Prandtl number, Reynolds number and two within the definition of Sutherland's law; giving a total of 5 parameters.

In order to more accurately simulate flows under hypersonic conditions, a five species, two temperature nonequilibrium real gas model is considered. The species considered in this model are N_2,O_2,NO,N,and O and the two temperatures represent translation-rotation and vibrational-electronic energy respectively. For this model, the conserved variables and flux vectors are given by:[4]

$$\mathbf{U} = \left\{ \begin{array}{c} \rho_s \\ \rho\vec{u} \\ \rho e_t \\ \rho e_v \end{array} \right\} \quad \vec{F} = \left\{ \begin{array}{c} \rho_s\vec{u} \\ \rho\vec{u} \otimes \vec{u} + P \\ \rho\vec{u}h_t \\ \rho\vec{u}h_v \end{array} \right\} \quad \vec{F}_v = \left\{ \begin{array}{c} -\rho_s\tilde{V}_s \\ \underline{\tau} \\ \underline{\tau} \cdot \vec{u} - \vec{q} - \vec{q}_v - \sum_s h_{t,s}\rho_s\tilde{V}_s \\ -\sum_s h_{v,s}\rho_s\tilde{V}_s - \vec{q}_v \end{array} \right\}$$

In two dimensions, this model contains nine conserved variables. The first variable ρ_s is a local vector denoting the five species densities. The other variables are the bulk momentum, $\rho\vec{u}$, the total energy ρe_t, and the vibrational-electronic energy, ρe_v. In the absence of body forces and internal heat generation, the source vector for this model can be represented by:

$$\mathbf{S} = \left\{ \begin{array}{c} \omega_s \\ 0 \\ 0 \\ \sum_s \omega_s\hat{D}_{v,s} + Q_{T-V} \end{array} \right\} \tag{5}$$

In this vector, ω_s is the mass source for each of the species conservation equations and is determined based on the chemical reactions present in the flow. In addition to these reaction terms, the vibrational energy contains source terms relating to translational-vibrational energy coupling and energy changes due to chemical reactions.[4]

Like the perfect gas model, this model uses the assumption of a Newtonian fluid to construct the shear stress tensor and Fourier's law for the heat flux terms. The species diffusion velocities,$\tilde{V}_s$, are determined using Fick's law.

$$\rho_s\tilde{V}_s = -\rho D_s\nabla c_s \tag{6}$$

where c_s is the species mass fraction and D_s is the species diffusion coefficient. The model uses the ideal gas equation of state to calculate partial pressures due to each species and computes a total pressure via Dalton's Law.[5] Combining these two steps gives a state equation of the form:

$$P = \sum_s \rho_s \frac{\bar{R}}{M_s} T \tag{7}$$

where $\bar{R}$ is the universal gas constant and M_s is the species molecular weight. The chemical kinetics model used for this work is the Dunn-Kang two temperature model taken from reference.[6] The model includes dissociation reactions for the three diatomic species present in the model as well as two exchange reactions related to NO. When all dissociation partners are counted, there are a total of 17 distinct reactions. The Dunn-Kang model gives Arrhenius coefficients for the forward and backward reaction rates directly.[6] The translational-vibrational energy coupling term takes the form of a relaxation between the two respective temperatures with an empirically determined relaxation time, τ_s.[4]

$$Q_{T-V} = \sum_{s=ND} \frac{\rho_s C_{v,s}(T - T_v)}{< \tau_s >} \tag{8}$$

The transport properties required for this model are based upon curve fits for species viscosity developed by Blottner *et al*[7] and use a mixing rule due to Wilke[8] to determine bulk quantities.[5] Additionally, species diffusion coefficients are determined using the bulk transport quantities and the assumption of a constant Schmidt number across all species.[5] Finally, the specific heats are calculated via polynomial curve fits taken from reference.[4] These curve fits are a series of 4th order polynomials that cover various temperature ranges and represent the total specific heat for each species. The total enthalpy can be determined by simply integrating these curve fits and incorporating the proper heat of formation information.[4]

Embedded in the constitutive relations of this model are a number of experimentally measured parameters and correlations. Including the parameters required to define quantities like reaction rates, species specific heats, species viscosity and relaxation times, there are over 250 model parameters. One of the goals of this work is to quantify the effect these parameters have upon an objective of interest in an efficient and timely manner.

Before detailing the solution process used for this work, it is convenient to define a set of primitive variables for each model, denoted by $\mathbf{V}$. These primitive variables are used throughout the discretization process and the constitutive relations. For the perfect gas model, these primitive variables are density, velocity and temperature. For the real gas model, in addition to the primitive variables from the perfect gas model, species mass fractions and vibrational temperature are included as primitive variables.

II.B. Spatial Discretization

In order to solve problems using the above two models, a two dimensional cell-centered finite volume code was written. The governing equations described above are first discretized in space and the solution is advanced in time to steady state using a fully implicit approach. In semi-discrete form, the equations have the following form.

$$\frac{\partial \mathbf{U}}{\partial t} + \mathbf{R}(\mathbf{U}) = 0 \tag{9}$$

The residual within each cell is given by the sum of the normal inviscid and viscous flux over all faces plus a cell centered contribution due to source terms. The residual equation for cell i is given in equation (10) along with the functional dependence of each flux function.

$$\mathbf{R}_i(\mathbf{U}) = \sum_k \left[F_n^k(\mathbf{V}^+, \mathbf{V}^-, \vec{N}) - F_{v,n}^k(\mathbf{V}_L, \mathbf{V}_R, \nabla\mathbf{V}_L, \nabla\mathbf{V}_R, \vec{N}, \vec{T}) \right] + \mathbf{S}_i(\mathbf{V}_i) \tag{10}$$

In this equation, $\mathbf{V}_L$ and $\mathbf{V}_R$ represent cell centered primitive values for the cell to the left and the right of the face respectively. The variables $\mathbf{V}^+$ and $\mathbf{V}^-$ represent reconstructed primitive variables to the left and right of the face. The variables S_i represent the source terms computed using the cell centered primitive variables of cell i. Finally, $\vec{N}$ is the dimensional face normal and $\vec{T}$ represents the vector connecting the two cell centers on either side of the face. These terms are futher clarified in Figure 1.

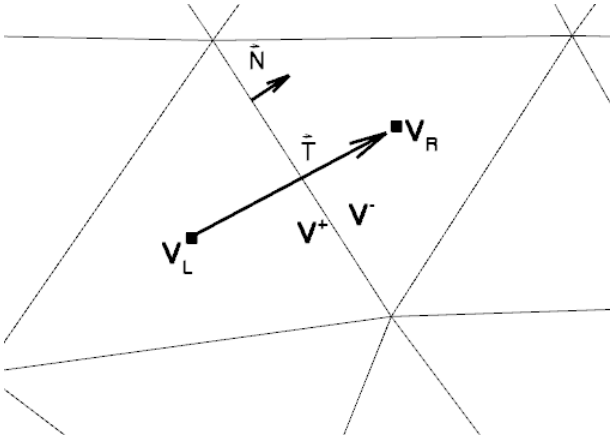

Figure 1. Variable definitions at mesh face

It should be noted that the flux functions and source term are defined exclusively in terms of the primitive variables, $\mathbf{V}$, instead of the conserved variables, $\mathbf{U}$. In addition to the cell centered primitive variables, the viscous flux is also a function of the cell centered gradients of the primitive variables. The choice of primitive variables as the inputs for these functions is due to two factors. First, the constitutive relations in the viscous flux are typically defined in terms of gradients of primitive variables. Additionally, by reconstructing and limiting primitive variables when calculating the inviscid flux, increased robustness of the solver is achieved and the need to calculate two sets of gradients is eliminated. The cell centered gradients are calculated using Green-Gauss contour integration. For the inviscid flux, F_n, the AUSM+UP flux function is used.[9] This flux function is chosen based on its applicability to a wide range of Mach numbers and the ease with which it can be extended to additional equations. For the real gas model, a frozen speed of sound is used within the inviscid flux function.[10] In order to achieve second order accuracy, the flux function is evaluated using the reconstructed primitive variables on each side of the face, denoted previously as $\mathbf{V}^+$ and $\mathbf{V}^-$. In order to maintain stability, a limiter is used in this reconstruction process. The limiter used within this code is a combination of a pressure switch and smooth Van Albada limiter, inspired by the experiences in references[5],[11] and.[10] The pressure switch in each cell is defined by:[12]

$$\nu_i = \frac{|\sum_k P_R - P_L|}{\sum_k P_R + P_L} \tag{11}$$

The limiter value at each face is defined by the continuous function Φ which assigns a limiter value given inputs dependent on the reconstructed value and neighboring cell centered values.[13]

$$\Phi(\Delta^+, \Delta^-) = \frac{1}{\Delta^-} \frac{(\Delta^{+^2} + \varepsilon^2)\Delta^- + 2\Delta^{-^2}\Delta^+}{\Delta^{+^2} + 2\Delta^- + \Delta^-\Delta^+ + \varepsilon^2} \tag{12}$$

where Δ^- and Δ^+ are defined as:

$$\Delta^- = \mathbf{V}_k - \mathbf{V}_i \tag{13}$$

$$\Delta^+ = \begin{cases} \mathbf{V}_{max} - \mathbf{V}_i & \text{if } \mathbf{V}_k - \mathbf{V}_i > 0 \\ \mathbf{V}_{min} - \mathbf{V}_i & \text{if } \mathbf{V}_k - \mathbf{V}_i < 0 \end{cases} \tag{14}$$

and $\mathbf{V}_k$ is the unlimited reconstructed face value, $\mathbf{V}_i$ is the cell centered value and $\mathbf{V}_{min}$ and $\mathbf{V}_{max}$ represent the minimum and maximum values surrounding cell i. The parameter ε reduces the limiter sensitivity to small changes in the flow, effectively forcing the limiter to unity in smooth regions. This reduced sensitivity allows the limiter to achieve convergence to machine zero provided the parameter is high enough.[13] Unfortunately, this improved convergence tends to come at the price of robustness. Hence, the pressure switch is included in the limiter to ensure the solution is first order in the presence of strong shocks. Outside of this small region, the limiter is allowed to adjust the reconstruction. In functional form, the final limiter at each face takes the form:

$$\mathbf{\Psi}_k = max(0, 1 - Kmax(\nu_L, \nu_R))\tilde{\mathbf{\Psi}}_k \tag{15}$$

where $\tilde{\mathbf{\Psi}}_k$ is the result of applying the function Φ at each face with the proper inputs and K is a prescribed constant used to set the minimum value of the pressure switch required to force the limiter to zero. The cell centered limiter value is taken to be the minimum of the limiters calculated at each face of the cell. With the limiter calculated, the reconstructed value at each face is given by:

$$\mathbf{V}^+ = \mathbf{V}_L + \mathbf{\Psi}_L \nabla \mathbf{V}_L \cdot \Delta \vec{X}_L \tag{16}$$

$$\mathbf{V}^- = \mathbf{V}_R + \mathbf{\Psi}_R \nabla \mathbf{V}_R \cdot \Delta \vec{X}_R \tag{17}$$

where $\Delta \vec{X}_L$ and $\Delta \vec{X}_R$ are connecting the face center with the left and right cell centers respectively. The calculation of the viscous flux is relatively straight forward. Each term in the viscous flux from equation (10) is calculated using face centered quantities. In the case of any primitive variables, a simple average of the left and right states is used and transport quantities are calculated using this averaged state. Face-based gradients are calculated through the following equation which ensures a coupling between neighboring cells and a straight forward approximate linearization:[14]

$$\nabla \mathbf{V}_k = \tilde{\nabla \mathbf{V}} + \frac{\mathbf{V}_R - \mathbf{V}_L - \tilde{\nabla \mathbf{V}} \cdot \Delta T}{|\Delta T|} \frac{\Delta T}{|\Delta T|} \tag{18}$$

In this equation, $\tilde{\nabla \mathbf{V}}$ is a simple average of the left and right cell centered gradients and the vector ΔT is defined as before.

II.C. Solution Procedure

The result of the spatial discretization described above is a system of coupled ordinary differential equations. These ODE's are solved to steady-state using the BDF1 temporal discretization given by:

$$\frac{\partial \mathbf{U}}{\partial t} \approx \frac{\mathbf{U}^n - \mathbf{U}^{n-1}}{\Delta t} \tag{19}$$

The result of this temporal discretization is a system of nonlinear equations which must be solved at each time step. These nonlinear equations are represented by the unsteady residual $\mathbf{J}$.

$$\mathbf{J}(\mathbf{U}^n, \mathbf{U}^{n-1}) = \frac{\mathbf{U}^n - \mathbf{U}^{n-1}}{\Delta t} + \mathbf{R}(\mathbf{U}^n) = 0 \tag{20}$$

To solve this nonlinear equation, an approximate Netwon's method is employed. In general, a Newton's method for this problem would take the following form:

$$\delta \mathbf{U}^k = -\left[\frac{\partial \mathbf{J}(\mathbf{U}^k, \mathbf{U}^{n-1})}{\partial \mathbf{U}^k}\right]^{-1} \mathbf{J}(\mathbf{U}^k, \mathbf{U}^{n-1}) \tag{21}$$

$$\mathbf{U}^{k+1} = \mathbf{U}^k + \delta \mathbf{U}^k \tag{22}$$

Within this general form, several approximations are introduced to increase the robustness of the solver and improve its applicability to steady problems. First, instead of fully converging the nonlinear problem, only a set number of Newton iterations is performed per time step (typically 10). In order to speed convergence of steady problems, local time stepping can be used within this formulation although robustness can be negatively affected. Typically, global time stepping is used to partially converge the problem and local time stepping is used to achieve full convergence. Second, to decrease the time required per Newton iteration, the exact Jacobian matrix is replaced by a preconditioning matrix that is calculated once at the beginning of the time step and frozen for the duration of the time step. Typically, this preconditioning matrix is based upon a robust and easy to calculate Jacobian. Finally, transport quantities such as viscosity, thermal conductivity and species diffusion coefficients are frozen within the Newton iterations to further decrease computational cost. Incorporating these simplifications, the subiterations within each timestep take the following form.

$$\delta \mathbf{U}^k = -[\tilde{P}]^{-1} J(\mathbf{U}^k, \mathbf{U}^{n-1}) \tag{23}$$

$$\mathbf{U}^{k+1} = \mathbf{U}^k + \lambda \delta \mathbf{U}^k \tag{24}$$

In these equations, $[\tilde{P}]$ is the frozen preconditioning matrix and the variable λ is used to ensure that updates remain within a specified percentage of the previous solution value.[15] The form of the preconditioning matrix depends on the problem being solved and the amount of nonlinearity present in the problem. For numerically stiff problems, or for starting a problem, the preconditioner matrix is taken as the diagonal of the 1st order Van-Leer-Hänel Jacobian and is inverted in the block-wise sense.[16] For less stiff or partially converged problems, a colored Gauss-Seidel or line-implicit solver is used to advance the Newton iteration within each time step in a quasi-nonlinear fashion. For these cases, the full 1st order Van-Leer-Hänel Jacobian, including off-diagonal elements, is required.

III. Sensitivity Procedure

To determine the sensitivity of an objective to the input parameters, the code is differentiated and the final sensitivity is constructed using the chain rule. To illustrate this process, the following objective and functional dependence are considered.

$$L = L(D, \mathbf{U}(D)) \tag{25}$$

$$\tag{26}$$

In addition to this objective, a constraint is needed. For the steady problems considered in this work, the constraint is that the spatial residual must equal zero.

$$\mathbf{R}(D, \mathbf{U}(D)) = 0 \tag{27}$$

Both the constraint and the residual have an explicit dependence on the input parameter, or design variable D, and an implicit dependence through the flow variables $\mathbf{U}$. In order to determine the sensitivity derivative, the objective can be differentiated using the chain rule as:[17]

$$\frac{dL}{dD} = \frac{\partial L}{\partial D} + \frac{\partial L}{\partial \mathbf{U}} \frac{\partial \mathbf{U}}{\partial D} \tag{28}$$

The constraint may be differentiated in a similar manner. In this case, the derivative is equal to zero as the constraint must be satisfied for all admissible values of D and $\mathbf{U}$:

$$\frac{\partial \mathbf{R}}{\partial D} + \frac{\partial \mathbf{R}}{\partial \mathbf{U}} \frac{\partial \mathbf{U}}{\partial D} = 0 \tag{29}$$

Solving for $\frac{\partial \mathbf{U}}{\partial D}$ in the above equation and substituting into the objective derivative gives the forward sensitivity equation.

$$\frac{dL}{dD} = \frac{\partial L}{\partial D} - \frac{\partial L}{\partial \mathbf{U}} \frac{\partial \mathbf{R}}{\partial \mathbf{U}}^{-1} \frac{\partial \mathbf{R}}{\partial D} \tag{30}$$

The adjoint sensitivity equation is found by taking the transpose of the forward equation.

$$\frac{dL}{dD}^T = \frac{\partial L}{\partial D}^T - \frac{\partial \mathbf{R}}{\partial D}^T \frac{\partial \mathbf{R}}{\partial \mathbf{U}}^{-T} \frac{\partial L}{\partial \mathbf{U}}^T \tag{31}$$

where the last two terms can be replaced by the adjoint variable $\mathbf{\Lambda}$, defined as:

$$\frac{\partial \mathbf{R}}{\partial \mathbf{U}}^T \mathbf{\Lambda} = -\frac{\partial L}{\partial \mathbf{U}}^T \tag{32}$$

Determining the solution of the flow adjoint equation is the most expensive step of the sensitivity process and roughly follows the procedure used to solve the analysis problem. A simplified preconditioner matrix is used to advance the adjoint solution in a defect-correction scheme.[17] A defect correction scheme for the adjoint solve can be represented as:

$$[P]^T \delta \mathbf{\Lambda}^k = -\frac{\partial L}{\partial \mathbf{U}}^T - \frac{\partial \mathbf{R}}{\partial \mathbf{U}}^T \mathbf{\Lambda}^k \tag{33}$$

$$\mathbf{\Lambda}^{k+1} = \mathbf{\Lambda}^k + \delta \mathbf{\Lambda}^k \tag{34}$$

where $[P]$ is the same preconditioner used for the flow problem and the defect-correction scheme is advanced in a similar manner to the flow problem, using an element Jacobi, colored Gauss-Seidel or line implicit method. Unfortunately, due to the nonlinear nature of hypersonic flows, this defect correction scheme can suffer from the same start up problems which affect the flow problem. To overcome this problem, a pseudo-time component is added to the preconditioner matrix. When the problem is posed in this defect-correction form, only the effect of the adjoint on the exact transposed Jacobian is required. This type of formulation is ideally suited for use with automatic differentiation, which forms derivatives as a matrix-vector product instead of computing individual elements of the Jacobian directly. By using automatic differentiation, a general defect correction scheme can be implemented and individual automatically differentiated subroutines can be used to build up the effect of the full transposed Jacobian piece by piece. This approach adds a degree of modularity and maintainability to the adjoint sensitivity process. The automatic differentiation used in this work is provided by the Tapenade Automatic Differentiation Engine.[18] The majority of the terms needed to calculate the sensitivity were generated via automatically differentiated subroutines and constructed as a chain of matrix-vector products. In this way, few matrices need to be stored. The only matrix computed and stored is the preconditioner matrix $[P]$, which is needed for both the flow problem and the adjoint problem.

Finally, with the flow adjoint computed and the appropriate partial derivatives determined, the final sensitivity can be calculated with the equation:

$$\frac{dL}{dD} = \frac{\partial L}{\partial D} + \frac{\partial \mathbf{R}}{\partial D}^T \mathbf{\Lambda} \tag{35}$$

The adjoint sensitivity procedure has the advantage of including the design variable as the last step in the process. As such, a single adjoint solution can be used to compute the sensitivity of a single objective to any number of design variables. At this point, the definition of a design variable should be viewed in an encompassing manner, including any input variable required to define the numerical problem. For shape optimization, the design variable may take the form of point displacements or variables used for the parametric definition of the geometry. For simulation optimization, the design variable may be a simulation parameter such as a limiter constant or pressure-switch threshold. For uncertainty quantification, the design variable may be a model parameter, curve fit quantity or any other quantity with a related uncertainty. Fortunately, the same adjoint can be used for all of these different design variables provided the same quantities are held constant within the adjoint solve.

In order to demonstrate the sensitivity process, the sensitivity for various different classes of design variables will be explained. In the case of geometric sensitivity, the dependence of the objective and residual on mesh geometry must be considered. Consider the following functional dependence:

$$L = L(\mathbf{U}(\mathbf{X}(D)), \mathbf{X}(D)) \tag{36}$$

$$\mathbf{R} = \mathbf{R}(\mathbf{U}(\mathbf{X}(D)), \mathbf{X}(D)) \tag{37}$$

where $\mathbf{X}$ represents the coordinates of the nodes in the computational mesh.

The forward sensitivity equation for this type of functional dependence can be written as:[19]

$$\frac{dL}{dD} = \frac{\partial L}{\partial \mathbf{X}} \frac{\partial \mathbf{X}}{\partial D} - \frac{\partial L}{\partial \mathbf{U}} \left[\frac{\partial \mathbf{R}}{\partial \mathbf{U}}\right]^{-1} \frac{\partial \mathbf{R}}{\partial \mathbf{X}} \frac{\partial \mathbf{X}}{\partial D} \tag{38}$$

The adjoint sensitivity equation is found by taking the transpose of the above equation and using the definition of the flow adjoint from equation 32.

$$\frac{dL}{dD} = \frac{\partial \mathbf{X}}{\partial D}^T \left(\frac{\partial L}{\partial \mathbf{X}}^T - \frac{\partial \mathbf{R}}{\partial \mathbf{X}}^T \mathbf{\Lambda} \right) \tag{39}$$

The vector $\frac{\partial \mathbf{X}}{\partial D}$ represents the relationship between the design variable and the mesh coordinates. The complexity of this term varies depending on the design variable being considered as well as the geometric relationship, if any, between nodes in the mesh. If the design variable is taken to be a point in the mesh, then this term reduces to what is essentially a Kronecker delta function. If a mesh deformation strategy is employed, such as a spring analogy, this term will require the solution of the linearized deformation equations to determine the dependence of the mesh coordinates on the design variable.[17]

Next, consider the problem of determining the sensitivity to a set of model parameters. Let α represent a set of model parameters in the code. Model parameters typically enter the solution process through the constitutive relations used to specify the physical quantities needed to solve the flow, such as viscosity, specific heat, thermal conductivity, etc. Let the intermediate quantities associated with the parameters α be denoted by the vector $\boldsymbol{\mu}$ where μ_i represents the intermediate quantity at the appropriate location in the computational mesh, such as at cell centers for source terms and at face centers for flux terms. This intermediate quantity is typically a function of local flow conditions as well as the model parameters. For example, Sutherland's law can be written as:

$$\frac{\mu}{\mu_{ref}} = \frac{C_1 T^{3/2}}{T + S} \tag{40}$$

where C_1, S and μ_{ref} would be considered elements within the vector α and the intermediate variable would be the viscosity. Since the viscosity is required to compute the viscous flux, the intermediate variable vector would consist of the face-centered viscosities throughout the mesh.

To determine the sensitivity of an objective to any of the variables in the parameter vector, the following functional dependence should be considered:

$$L = L(\mathbf{U}(\alpha), \boldsymbol{\mu}(\alpha, \mathbf{U}(\alpha))) \tag{41}$$

$$\mathbf{R} = \mathbf{R}(\mathbf{U}(\alpha), \boldsymbol{\mu}(\alpha, \mathbf{U}(\alpha))) \tag{42}$$

The forward sensitivity associated with this functional dependence is given by:

$$\frac{dL}{d\alpha} = \frac{\partial L}{\partial \boldsymbol{\mu}} \frac{\partial \boldsymbol{\mu}}{\partial \alpha} + \left(\frac{\partial L}{\partial \mathbf{U}} + \frac{\partial L}{\partial \boldsymbol{\mu}} \frac{\partial \boldsymbol{\mu}}{\partial \mathbf{U}} \right) \frac{\partial \mathbf{U}}{\partial \alpha} \tag{43}$$

where $\frac{\partial \mathbf{U}}{\partial \alpha}$ is determined by solving the equation:

$$\left[\frac{\partial \mathbf{R}}{\partial \mathbf{U}} + \frac{\partial \mathbf{R}}{\partial \boldsymbol{\mu}} \frac{\partial \boldsymbol{\mu}}{\partial \mathbf{U}} \right] \frac{\partial \mathbf{U}}{\partial \alpha} = - \frac{\partial \mathbf{R}}{\partial \boldsymbol{\mu}} \frac{\partial \boldsymbol{\mu}}{\partial \alpha} \tag{44}$$

The corresponding adjoint equation for this functional dependence is:

$$\left[\frac{\partial \mathbf{R}}{\partial \mathbf{U}} + \frac{\partial \mathbf{R}}{\partial \boldsymbol{\mu}} \frac{\partial \boldsymbol{\mu}}{\partial \mathbf{U}} \right]^T \boldsymbol{\Lambda} = - \left(\frac{\partial L}{\partial \mathbf{U}}^T + \frac{\partial \boldsymbol{\mu}}{\partial \mathbf{U}}^T \frac{\partial L}{\partial \boldsymbol{\mu}}^T \right) \tag{45}$$

Using this adjoint, the final parameter sensitivity is given by:

$$\frac{\partial L}{\partial \alpha}^T = \frac{\partial \boldsymbol{\mu}}{\partial \alpha}^T \left(\frac{\partial L}{\partial \boldsymbol{\mu}}^T + \frac{\partial \mathbf{R}}{\partial \boldsymbol{\mu}}^T \boldsymbol{\Lambda} \right) \tag{46}$$

Instead of calculating the sensitivity to α, the sensitivity with respect to the intermediate quantity $\boldsymbol{\mu}$ could also be calculated. This results in merely a specialized case of the general parameter sensitivity where $\frac{\partial \boldsymbol{\mu}}{\partial \alpha} = 1$ and $\frac{\partial \boldsymbol{\mu}}{\partial \mathbf{U}} = 0$. The adjoint sensitivity equation for a particular μ_i can be given by:

$$\frac{\partial L}{\partial \mu_i} = \boldsymbol{\delta_i} \left(\frac{\partial L}{\partial \boldsymbol{\mu}}^T + \frac{\partial R}{\partial \boldsymbol{\mu}}^T \boldsymbol{\Lambda} \right) \tag{47}$$

where $\boldsymbol{\delta_i}$ is a vector with an entry of unity for the ith component and zero elsewhere. The adjoint equation for this case is given by:

$$\left[\left(\frac{\partial \mathbf{R}}{\partial \mathbf{U}} \right)_{\boldsymbol{\mu}} \right]^T \boldsymbol{\Lambda} = - \frac{\partial L}{\partial \mathbf{U}}^T \tag{48}$$

It should be noted that this flow adjoint is solved with the intermediate value frozen. As such, it is a different adjoint then the one used to determine sensitivities with respect to α. Although a specialized adjoint is needed, this approach gives the sensitivity with respect to all of the intermediate variables in the computational mesh with a single adjoint solve. If the intermediate quantities are stored at the cell centers,

the number of sensitivities needed is proportional to the number of cells in the mesh. Calculating sensitivities with respect to intermediate values may prove useful for determining regions of the flow field and/or field value ranges that have the largest effect on the objective of interest. This, in turn, may enable adaptive modeling techniques or enhanced uncertainty quantification strategies. For example, the uncertainty in surface heating due to the quantities $\boldsymbol{\mu}$ could be calculated as:[1]

$$\delta L^2 = \sum_i \frac{\partial L}{\partial \mu_i}^2 \delta \mu_i^2(\mathbf{U}_i) \tag{49}$$

By calculating uncertainty in this manner, the uncertainty associated with a particular μ_i can vary based on local flow variables such as temperature. In addition to uncertainty applications, the sensitivity with respect to an intermediate value may be used to drive a model adaptation process. In areas with low sensitivity, it may be possible to locally reduce the fidelity of the model to reduce computational expense, such as dropping higher order terms in a curve fit. In areas of high sensitivity, an improved version of the model may need to be implemented in order to improve the accuracy of the objective.

IV. Demonstration Results

IV.A. Perfect Gas Benchmark Results

In order to verify the code written for this work, the benchmark case given by reference[20] is considered. This benchmark uses a 5 km/s cylinder with a Reynolds number of 753,860 and a fixed wall temperature. The flow conditions used for this benchmark can be found in Table 1.

Table 1. Benchmark flow conditions

$V_\infty =$	5 km/s
$\rho_\infty =$	0.001 kg/m^3
$T_\infty =$	200 K
$T_{wall} =$	500 K
$M_\infty =$	17.605
$Re_\infty =$	753,860
$Pr_\infty =$	0.72

Results obtained with the current code are compared with the results produced by the well validated codes LAURA[3] and FUN2D.[20] Figure 2 shows a contour plot of the temperature throughout the domain. In addition to a contour plot, several stations along the cylinder are compared with the results of LAURA. Figure 3 shows the temperature along the stagnation streamline and within the boundary layer along the stagnation streamline. The shock standoff distance matches the distance predicted by LAURA. Additionally, the thermal boundary layer has the proper size and shape. In addition to comparing interior flow features, pressure coefficients and surface heating coefficients are compared in Figures 4 and 5. The code produces surface distributions in agreement with those produced by LAURA and FUN2D.

IV.B. Real Gas Results

To demonstrate the implementation of the real gas model presented previously, the same 5 km/s cylinder was considered. In addition to the fixed wall temperature encountered in the perfect gas benchmark, a supercatalytic wall was assumed for this problem. To ensure that the solver performed as anticipated, the results were compared to those produced by LAURA.[20] Figure 6 shows the translation-rotation temperature contour for this case. As expected, the shock standoff distance is lower and the temperature after the shock is reduced relative to the perfect gas results. In addition to contour plots, quantities along the stagnation streamline were examined. Figure 7 shows both translational and vibrational temperature along the stagnation streamline. Plotted along with these results are those produced by LAURA. The code produces temperature profiles in rough agreement with the LAURA results. Relative to the LAURA results, the code under predicts the temperature boundary layer thickness and over predicts the overshoots in both temperatures encountered at the shock. In addition to temperatures, the mass fractions along the stagnation streamline can be found in

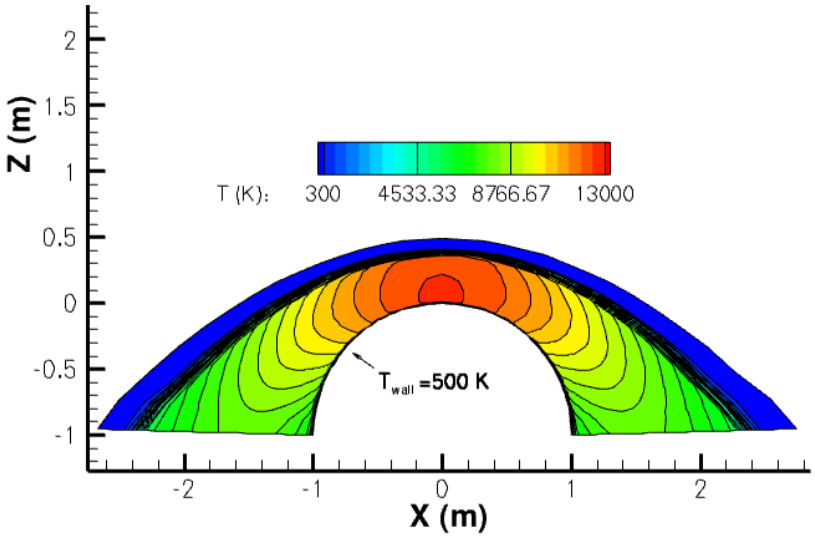

Figure 2. Temperature contour for 5 km/s perfect gas case

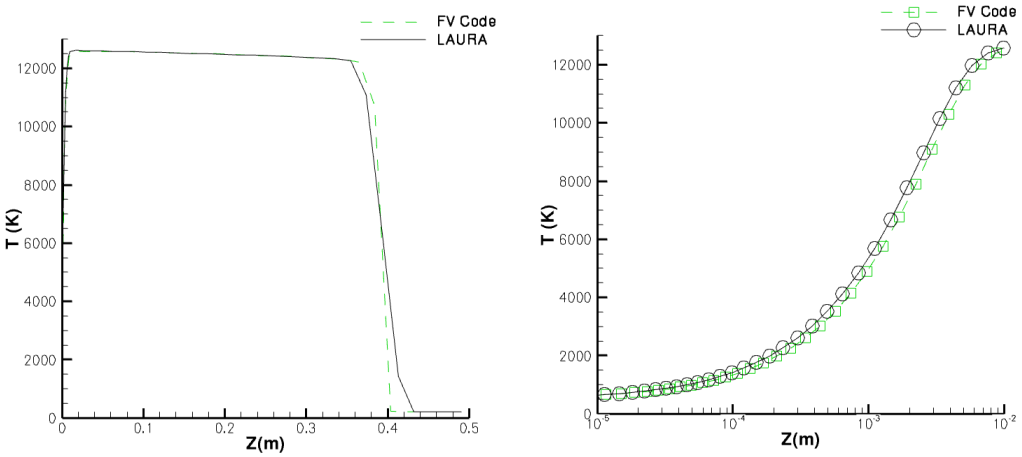

Figure 3. Temperature profile for 5 km/s perfect gas case (a) along stagnation streamline (b) within boundary layer

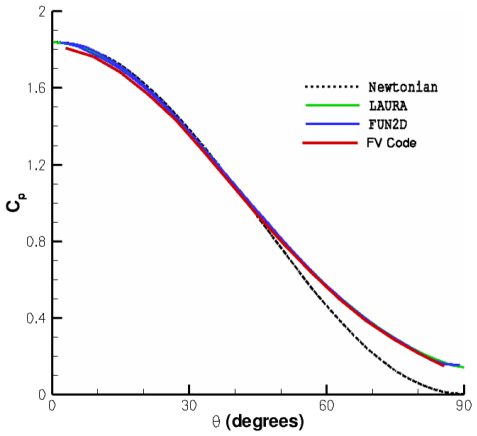

Figure 4. Surface pressure distribution for 5 km/s perfect gas case

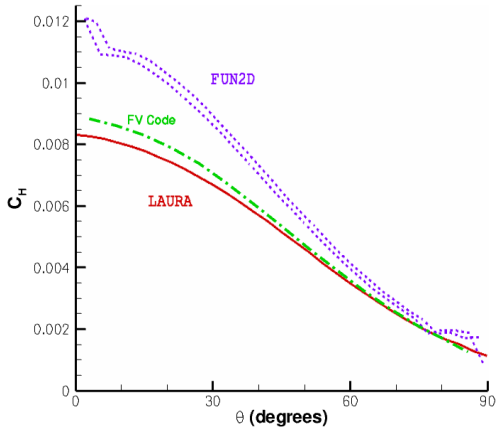

Figure 5. Surface heating distribution for 5 km/s perfect gas case

Figure 8. At the temperatures encountered in this case, oxygen is almost completely dissociated and nitrogen is beginning to dissociate. Although not shown, this behavior mimics the results produced by LAURA with some minor discrepancies present in the mass boundary layer. Finally, surface distributions were compared with the LAURA results. Figure 9 shows the surface pressure distribution while Figures 10 and 11 show the surface heating and skin friction respectively. As the plots show, the surface pressure and skin friction match the LAURA results relatively well but the surface heating is significantly under predicted.

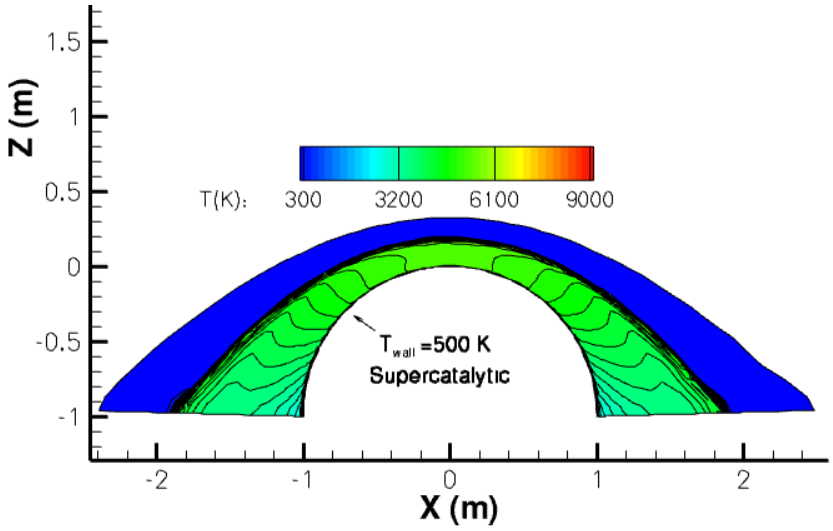

Figure 6. Temperature contour for 5 km/s real gas case

IV.C. Sensitivity for Perfect Gas Model

In order to test the sensitivity analysis capability of the code, the sensitivity of integrated surface heating to input variables is calculated for the benchmark problem described above. This objective is defined as:

$$L = -\int_{\partial\Omega} k\nabla T \cdot \vec{n} dA \tag{50}$$

where $\partial\Omega$ represents the solid surface, k is the thermal conductivity, T is the temperature and $\vec{n}$ is the outward facing unit normal of the surface.

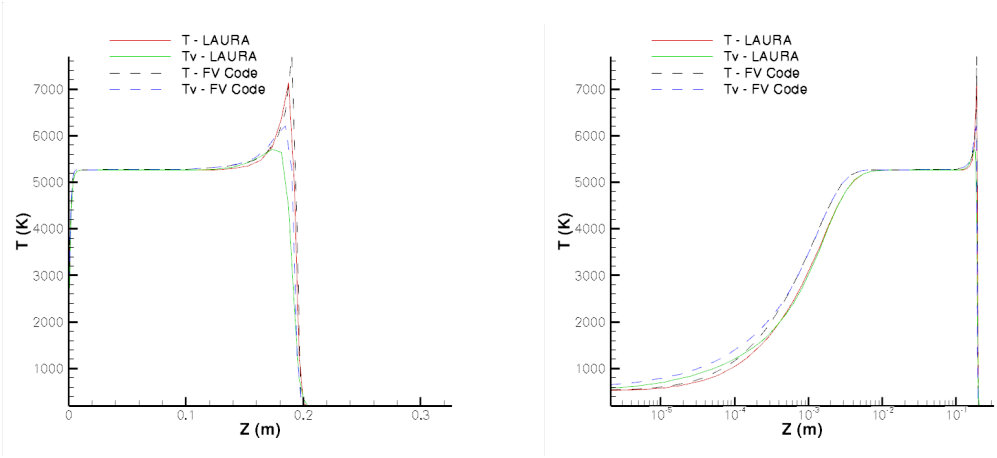

Figure 7. Temperature for 5 km/s real gas case a) along stagnation streamline b) along stagnation streamline on log scale

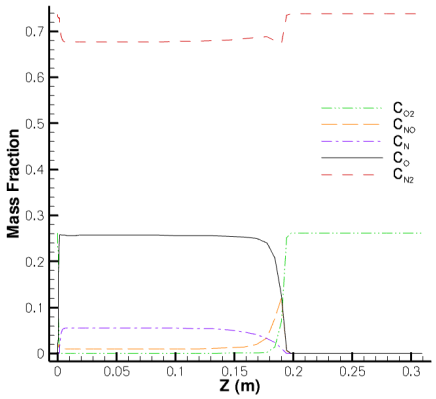

Figure 8. Mass fraction along stagnation streamline for 5 km/s real gas case

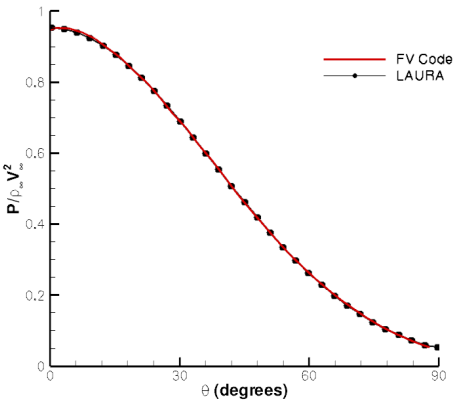

Figure 9. Surface pressure distribution for 5 km/s real gas case

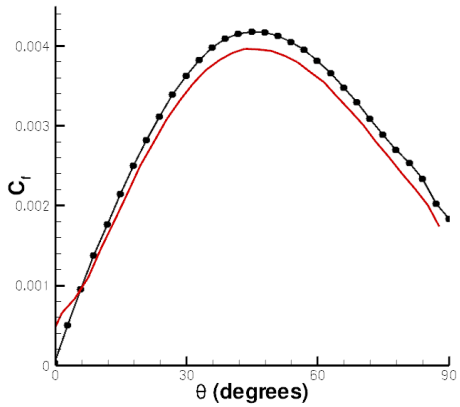

Figure 10. Skin friction distribution for 5 km/s real gas case

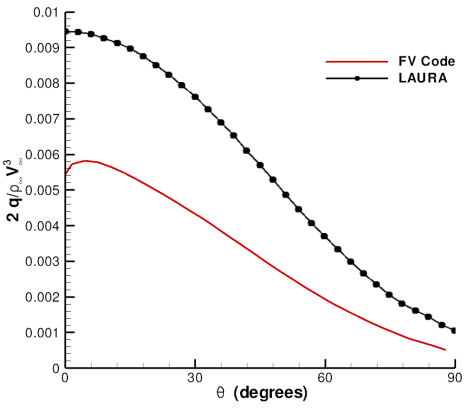

Figure 11. Surface heating distribution for 5 km/s real gas case

IV.C.1. Geometric Sensitivity

First, the sensitivity to surface point displacements was calculated. For this analysis, the design variable is taken to be the displacement of surface points normal to the cylinder's surface. The first step in calculating these sensitivities is to calculate the flow adjoint using integrated surface heating as the objective. The most interesting adjoint solution corresponds to density and is plotted in Figure 12.

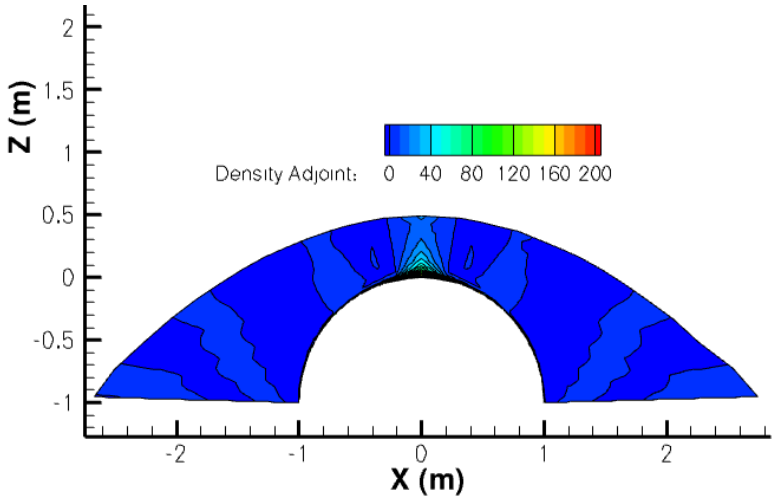

Figure 12. Density adjoint for integrated surface heating

As the adjoint solution shows, the cells close to the cylinder surface have the greatest importance for integrated surface heating calculations. In addition to the surface cells, the cells along the stagnation streamline are also of importance.

Using this adjoint, the sensitivity of the objective to normal displacements of the surface points is calculated. This sensitivity is plotted as a function of the angle along the cylinder in Figure 13. In order to verify the adjoint, finite difference is also used to calculate the same sensitivities and are plotted for comparison in Figure 13. In general, the adjoint produces sensitivities in agreement with finite difference. For some points, the disagreement between the two sensitivities becomes significant approaching 20% error. Although this may indicate an error in the adjoint sensitivity calculation, it could also be a symptom of the highly nonlinear nature of the problem. Through experimenting with the perturbation used in the finite difference, it was found that the value of the sensitivity varies widely as the perturbation is varied over a narrow band. For some points on the surface, the perturbation chosen may not be small enough to accurately calculate the sensitivity derivative. Unfortunately, as the perturbation decreases, machine error begins to pollute the sensitivity value. To more rigorously verify the sensitivity derivatives produced by the adjoint, complex differentiation will likely need to be employed.[21]

IV.C.2. Parameter Sensitivity

In addition to computing the sensitivity of surface heating to surface point placement, the sensitivity of surface heating to a physical parameter in the model was calculated. For the perfect gas model, the most interesting physical parameter is the ratio of the specific heats, γ. Because the same objective is being examined and the same variables are held fixed, the adjoint used for surface point sensitivities can be used to determine the sensitivity with respect to γ. As in the previous case, finite difference was again used to verify the sensitivity derivative produced by the adjoint. Two specific cases were considered for this sensitivity. First, the sensitivity was determined assuming a fixed freestream velocity. Second, a fixed freestream Mach number was assumed. The results of these two calculations are found in Table 2.

As the table shows, the adjoint sensitivity shows good agreement with the sensitivity found through finite difference. For both the fixed freestream velocity and Mach number, the integrated surface heating tends to decrease as γ increases. For the fixed freestream velocity, an increase in γ causes the freestream Mach number to decrease. This decrease in Mach number lowers the temperature after the shock and in turn lowers the integrated surface heating. For the fixed freestream Mach number, an increase in γ should tend

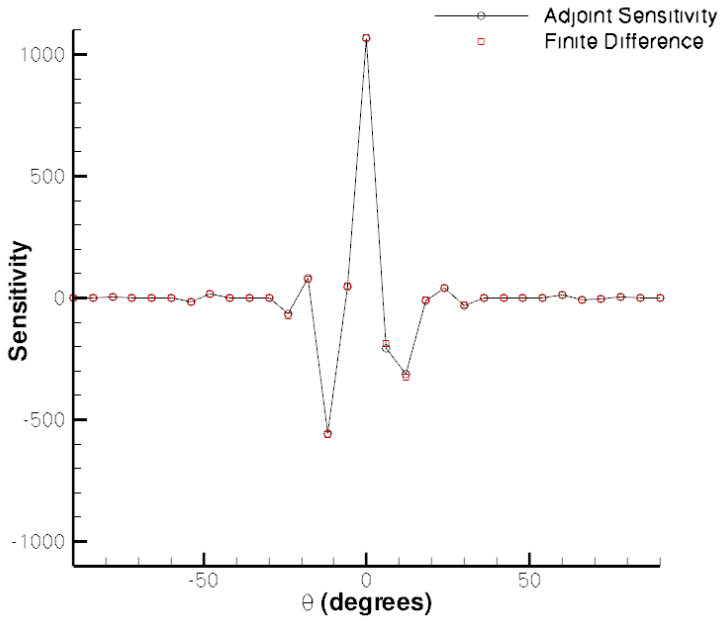

Figure 13. Sensitivity of surface heating to surface point displacements normal to surface for perfect gas model

Table 2. Sensitivity of surface heating to γ

	Fixed Velocity	Fixed Mach Number
Objective Value	1.628×10^{-2}	1.628×10^{-2}
Finite Difference	-3.111×10^{-2}	-1.198×10^{-2}
Adjoint	-3.109×10^{-2}	-1.206×10^{-2}
Relative Error	7.279×10^{-4}	7.186×10^{-4}

to increase the temperature after the shock. However, an increase in γ also causes the Prandtl number to increase which most likely increases the thickness of the boundary layer. From these results, it is clear that this viscous effect appears to more than off-set the increase in post-shock temperature expected from an increase in γ.

IV.D. Sensitivity for Real Gas model

To demonstrate the sensitivity capability of the solver for more complex problems, the sensitivity of surface heating to various parameters for the real gas model were computed. For the real gas model, the objective is defined as:

$$L = -\int_{\partial\Omega} k\nabla T \cdot \vec{n} + k_v \nabla T_v \cdot \vec{n} dA \tag{51}$$

where T and T_v represent translational-rotational and vibrational-electronic temperature respectively, k and k_v are the thermal conductivities for the two temperatures, and $\partial\Omega$ and $\vec{n}$ are defined as before.

IV.D.1. Geometric Sensitivity

The first sensitivity examined was the sensitivity of surface heating to geometric parameters. The design variable in this case was chosen as normal displacements of surface nodes in the mesh. The sensitivity as a function of angle along the cylinder is plotted in Figure 14, where it is compared to the corresponding finite difference values, showing good overall agreement.

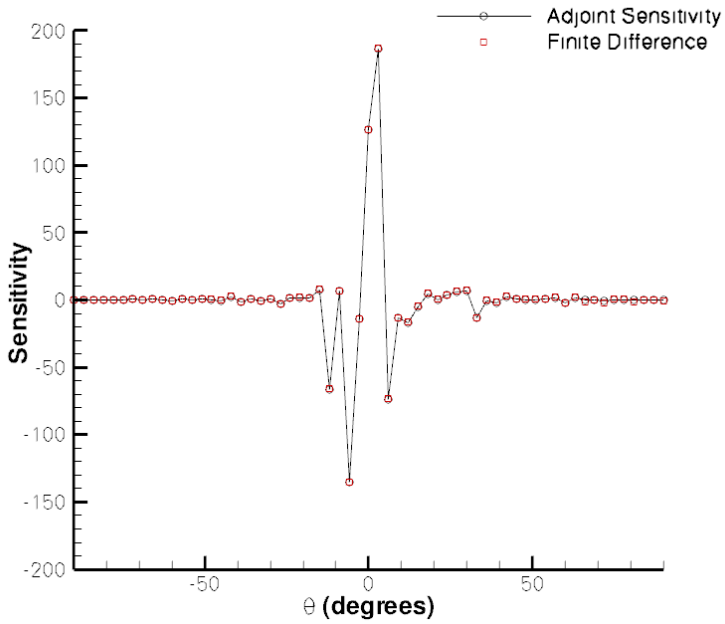

Figure 14. Sensitivity of surface heating to normal displacements for real gas case

IV.D.2. Parameter Sensitivity

In addition to geometric sensitivity, the sensitivity of surface heating to various model parameters was examined. As alluded to previously, the real gas model contains a number of empirically determined constitutive relations. Within these relations are a number of constants and curve fit parameters that help define the relationship. For the model implemented in this work, approximately 250 parameters are required. The sensitivity to several of these parameters is presented below.

The first set of parameters examined relates to the definition of reaction rate within the Dunn and Kang chemical kinetics model. For this model, the forward and backward reaction rates are defined via an Arrhenius equation:

$$K_f = C_f T_a^{\eta_f} e^{-\frac{E_{a,f}}{kT_a}} \tag{52}$$

$$K_b = C_b T_a^{\eta_b} e^{-\frac{E_{a,b}}{kT_a}} \tag{53}$$

where $E_{a,f}$ and $E_{a,b}$ represent the activation energy for the forward and backward reactions respectively, k is Boltzmann's constant and T_a is a characteristic temperature. The parameters examined were C_f and C_b for each reaction. For this model, there are 17 unique reactions, giving a total of 34 parameters. The bar graph below contains the sensitivities for each of these parameters. Due to the large discrepancy between the design variable and the objective, the sensitivity is expressed as fractional change in objective per fractional change in design variable (i.e. $\frac{\frac{dL}{L}}{\frac{dD}{D}}$).

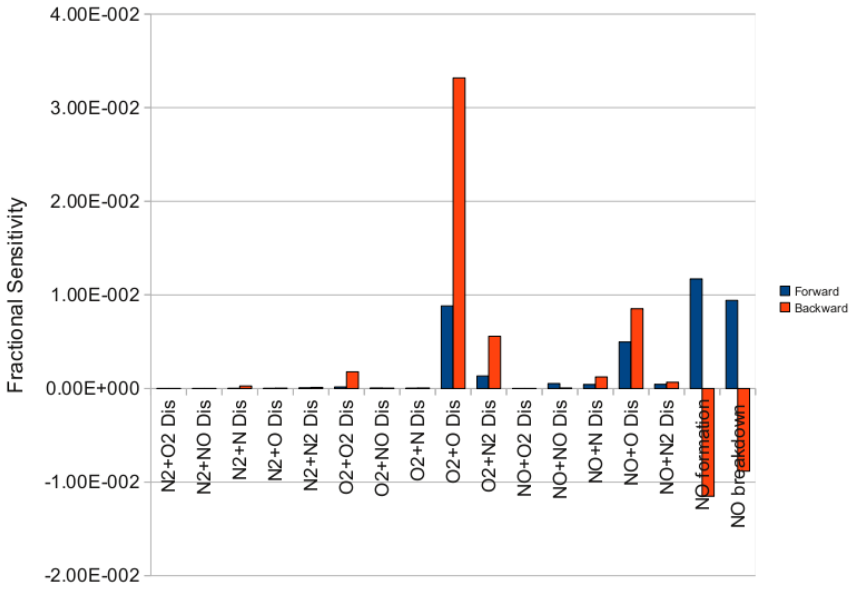

Figure 15. Sensitivity of surface heating to reaction parameters

As the graph demonstrates, the reactions governing the creation and breakdown of Nitrous-oxide seem to be the most important reactions in terms of sensitivities for determining surface heating. Additionally, the parameters governing the dissociation and recombination of diatomic oxygen are also of significance. These sensitivity numbers only quantify the importance of these parameters and say nothing regarding the overall uncertainty with respect to surface heating arising from these reactions. The uncertainty arising from these parameters would depend both on the sensitivity derivative and the uncertainty associated with the parameter itself. In the case of reaction rates, the associated uncertainty can be ± 1 order of magnitude, which may componsate for the relatively low sensitivity and give a significant overall contribution to uncertainty.[22]

In addition to reaction parameters, the sensitivities to parameters within the energy coupling term were calculated. Within the energy coupling term, an empirically defined interspecies relaxation time is required. This interspecies relaxation time is determined by the following equation:[4]

$$\tau_s^{MW} = \frac{\sum_{j=1}^{ns} n_j e^{A_s(T^{-1/3} - 0.015\mu_{s,j}^{1/4}) - 18.42}}{\sum_{j=1}^{ns} n_j} \tag{54}$$

where n_j is the species number density and $\mu_{s,j}$ is the reduced mass. The parameter A_s is defined for each diatomic species, giving 3 parameters for this model. The sensitivity of surface heating to these 3 parameters can be found in the table below.

Table 3. Sensitivity of surface heating to energy coupling parameter

	Value	Sensitivity $(\frac{\frac{dL}{L}}{\frac{dD}{D}})$
O_2	129	-3.31×10^{-5}
NO	168	-4.32×10^{-5}
N_2	220	-3.55×10^{-3}

As the table shows, the most important of these parameters is associated with diatomic nitrogen. Intuitively, this result makes sense as it is the most prevalent diatom present after the shock and it is directly after the shock that the problem exhibits the highest level of thermal nonequilibrium. Relative to the reaction parameters, those associated with energy coupling rank somewhere in the middle in terms of importance.

Finally, the sensitivity to parameters associated with transport quantities was examined. The calculation of transport terms rely on curve fits for species viscosity of the form:[5]

$$\mu_s = 0.1e^{(A_s ln(T)+B_s)ln(T)+C_s} \tag{55}$$

Associated with each species are the parameters A_s,B_s, and C_s, giving a total of 15 parameters for this model. The sensitivity for each of these parameters can be found in the graph below.

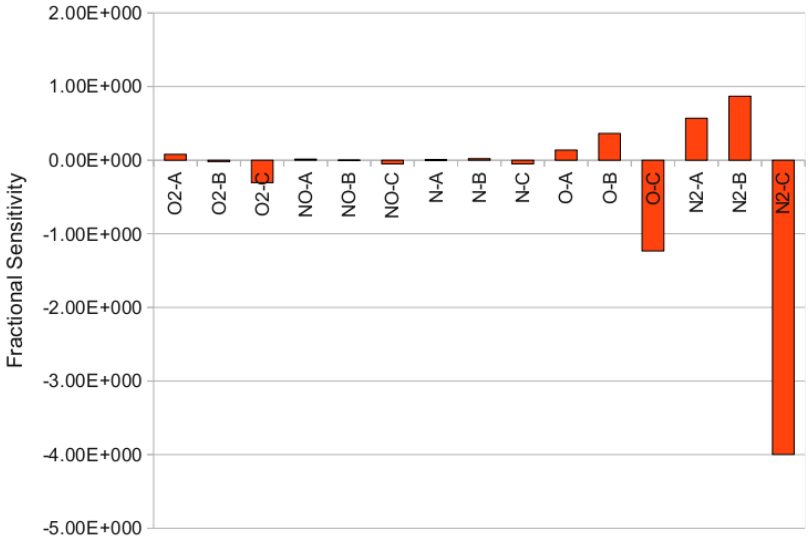

Figure 16. Sensitivity of surface heating to transport parameters

As the graph demonstrates, the sensitivity associated with these transport parameters is significantly higher than any other parameter analyzed in this paper. Of particular interest is the variable C associated with diatomic nitrogen and monoatomic oxygen. These two parameters are by far the most important to surface heating for this problem. Monte Carlo based approaches have also found transport quantities to have the highest contribution to surface heating for flow conditions similar to those examined here,[2].[22]

IV.D.3. Flow Field Variable Sensitivity

Finally, as a proof of concept, the uncertainty of integrated surface heating to the viscosity throughout the domain was determined. For the discretization outlined in this work, viscosity is needed at each face in the domain. In order to facilitate the sensitivity process, the viscosity was precomputed and stored at the faces. Hence in the terminology presented previously, the vector $\boldsymbol{\mu}$ holds the face-centered viscosities for the

entire grid. As explained previously, this sensitivity requires an adjoint solution found by holding viscosity constant. Using this exact adjoint, the sensitivity to face-centered viscosities was computed and is plotted in Figure 17. In order to plot the sensitivity, the face-centered quantities sensitivities were averaged over each cell.

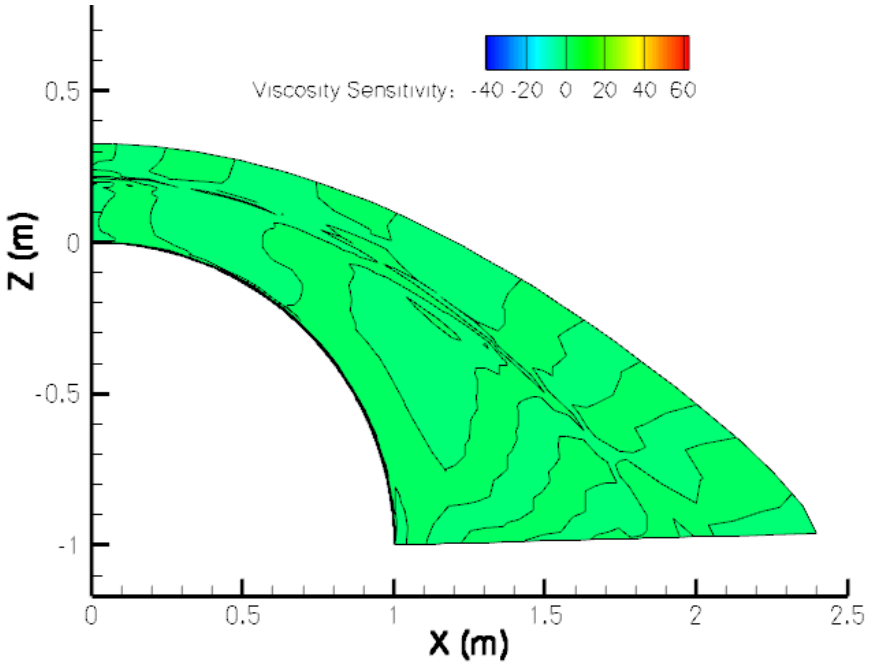

Figure 17. Sensitivity of surface heating to viscosity throughout domain

As the plot shows, the sensitivity to viscosity is essentially zero except in the vicinity of the boundary layer and the shock. Near the surface of the cylinder, the sensitivity becomes non-zero and increases in magnitude as the angle along the cylinder is increased. Intuitively, this results makes sense as the sensitivity to viscosity should increase as the velocity boundary becomes fully developed. In addition to the contour plot, the viscosity sensitivities along the stagnation streamline and the 45 degree station are plotted in Figures 18 and 19. As the Figures indicate, the overall magnitude of the sensitivity is larger for the 45 degree station than along the stagnation streamline. Additionally, the sensitivity changes signs within the boundary layer. Because the mass species diffusion is determined by assuming a constant Schmidt number, this change in sign most likely relates to the overlap between the momentum and mass boundary layers. In order to validate these results, the sensitivity was checked at several places in the domain using finite difference. These results can be found in Table IV.D.3. As the table shows, the agreement with finite difference is generally good and the disagreement is most likely caused by the limitations of finite difference.

In addition to using the exact adjoint, the same adjoint used for the geometric and parameter sensitivities was used to calculate the sensitivity to viscosity. This approximate adjoint produced results nearly identical to the sensitivities computed using the true adjoint. For comparison, the approximate adjoint results are included in Figures 18 and 19 and Table IV.D.3. This outcome is promising as it opens up the possibility of using the same adjoint for all classes of design variables.

V. Conclusion and Future Work

In this paper, the use of the discrete adjoint to calculate sensitivity derivatives for viscous hypersonic flows was demonstrated. This work is performed within the context of a two dimensional cell-centered finite volume code and uses both a perfect gas and real gas model. For the perfect gas model, the code produces flow solutions which are nominally second order accurate and compare well with the results produced by LAURA and FUN2D. Additionally, real gas results were presented and compared reasonably with the results produced by LAURA. In order to demonstrate the applicability of the discrete adjoint procedure to viscous hypersonic flows, the sensitivities of integrated surface heating to different design variables were computed.

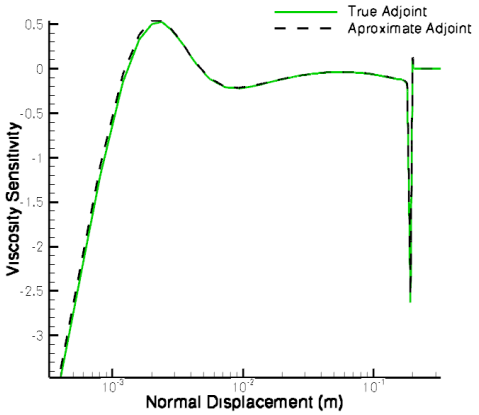

Figure 18. Sensitivity of surface heating to viscosity along the stagnation streamline

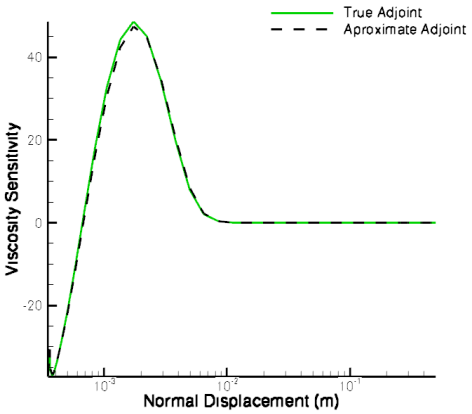

Figure 19. Sensitivity of surface heating to viscosity at 45 degrees

Table 4. Sensitivity of surface heating to viscosity at faces throughout the domain

Face	Exact Adjoint	Approximate Adjoint	Finite Difference ($\varepsilon = 10^{-3}$)
1	-10.149	-10.044	-9.691
1001	4.266×10^{-8}	1.149×10^{-7}	-4.654×10^{-4}
2001	4.343×10^{-3}	5.525×10^{-3}	3.766×10^{-3}
3001	-2.166×10^{-3}	-1.218×10^{-2}	-1.055×10^{-2}
4001	-3.185×10^{-2}	1.353×10^{-2}	8.466×10^{-4}
5001	5.667×10^{-2}	6.492×10^{-2}	6.989×10^{-4}
6001	1.176×10^{-2}	1.361×10^{-2}	1.610×10^{-4}
7001	2.506×10^{-3}	2.344×10^{-3}	1.082×10^{-4}

Initially, geometric sensitivities were examined for both the perfect gas and real gas models. Secondly, sensitivities of surface heating to a variety of parameters within the physical models were calculated. For the perfect gas model, the sensitivity with respect to γ was calculated. For the real gas model, the sensitivities to parameters relating to reaction rates, energy coupling and transport were calculated. When fractional changes of objective to fractional changes of input were compared, it was found that surface heating was most affected by transport parameters. It was also found that for this case, the reactions of greatest importance to surface heating were those governing the formation and breakdown of Nitrous Oxide and the recombination of oxygen. These sensitivities were validated using finite difference and showed good agreement. Finally, the sensitivity of an objective to a local field quantity was determined. For these calculations, the sensitivity to viscosity throughout the domain was calculated. Eventually, this local variable sensitivity may be used for uncertainty quantification or model adaptation.

Unfortunately, the adjoint approach outlined in this paper is limited in that it provides only a local estimate of the sensitivity derivative and may not properly account for nonlinear changes in sensitivity due to other input parameters.[1] In order to expand the applicability of these sensitivity derivatives, higher order terms, such as the sensitivity Hessian, will be included in the analysis.[23] Including these higher order terms should expand the range over which the adjoint approach is applicable. Additionally, in an attempt to capture the strengths of both approaches, hybrid sensitivity/sampling based techniques may be explored.

VI. Acknowledgments

This work is supported by the Department of Energy through the Computational Science Graduate Fellowship, administered through the Krell Institute.

References

[1]Michael J. Wright, D. B. and Chen, Y.-K., "Probabilistic Modeling of Aerothermal and Thermal Protection Material Response Uncertainties," *AIAA Journal*, Vol. 45, No. 2, February 2007.

[2]Palmer, G. E., "Uncertainty Analysis of CEV LEO and Lunar Return Entries," *39th AIAA Thermophysics Conference*, Miami, FL, June 2007.

[3]Cheatwood, F. M. and Gnoffo, P. A., "User's Manual for the Langley Aerothermodynamic Upwind Relaxation Algorithm (LAURA)," Tech. rep., NASA, April 1996.

[4]Peter A. Gnoffo, R. N. G. and Shinn, J. L., "Conservation Equations and Physical Models for Hypersonic Air Flows in Thermal and Chemical Nonequilibrium," Tech. rep., NASA, February 1989.

[5]Hassan, B., *Thermo-Chemical Nonequilibrium Effects on the Aerothermodynamics of Hypersonic Vehicles*, Ph.D. thesis, North Carolina State University, 1993.

[6]Dunn, M. G. and Kang, S.-W., "Theoretical and Experimental Studies of Reentry Plasmas," Tech. Rep. NASA CR-2232, NASA, April 1973.

[7]Blottner, F.G., J. M. and Ellis, M., "Chemically Reacting Gas Viscous Flow Program for Multi-Component Gas Mixtures," Tech. Rep. Sandia Release No. SC-RR-70-754, Sandia National Laboratories, Albuquerque, NM, December 1971.

[8]Wilke, C. R., "A Viscosity Equation for Gas Mixtures," *Journal of Chemical Physics*, Vol. 18, No. 4, March 1950, pp. 517–519.

[9]Liou, M.-S., "A sequel to AUSM, Part II: AUSM+-up for all speeds," *Journal of Computational Physics*, Vol. 214, 2006, pp. 137–170.

[10]Edwards, J. R., "A Low-Diffusion Flux-Splitting Scheme for Navier-Stokes Calculations," *Computers & Fluids*, Vol. 26, No. 6, 1997, pp. 635–659.

[11]Olynick, D. R., *A New LU-SGS Flow Solver for Calculating Reentry Flows*, Ph.D. thesis, North Carolina State University, 1992.

[12]Mavriplis, D. J., *Solution of the Two-Dimensional Euler Equations on Unstructured Triangular Meshes*, Ph.D. thesis, Princeton University, 1987.

[13]Venkatakrishnan, V., "Convergence to steady state solutions of the Euler equations on unstructured grids with limiters," *J. Comput. Phys.*, Vol. 118, No. 1, 1995, pp. 120–130.

[14]Jonathan M. Weiss, J. P. M. and Smith, W. A., "Implicit Solution of Preconditioned Navier-Stokes Equations Using Algebraic Multigrid," *AIAA Journal*, Vol. 37, No. 1, January 1999, pp. 29–36.

[15]Wang, L. and Mavriplis, D. J., "Implicit solution of the unsteady Euler equations for high-order accurate discontinuous Galerkin discretizations," *Journal of Computational Physics*, Vol. 225, 2007, pp. 1994–2015.

[16]Edwards, J. R., "Numerical Implementation of a Modified Liou-Steffen Upwind Scheme," *AIAA Journal*, Vol. 32, No. 10, 1994, pp. 2120–2122.

[17]Mavriplis, D., "Formulation and Multigrid Solution of the Discrete Adjoint for Optimization Problems on Unstructured Meshes," *43rd AIAA Aerospace Sciences Meeting*, Reno, NV, January 2005.

[18]INRIA Sophia-Antipolis, *The TAPENADE Tutorial*, March 2009.

[19]Mavriplis, D., "A Discrete Adjoint-Based Approach for Optimization Problems on Three-Dimensional Unstructured Meshes," *44th AIAA Aerospace Sciecnes Meeting and Exhibit*, Reno, NV, January 2006.

[20]NASA, *FUN3D: Fully Unstructured Navier-Stokes Manual*, May 2009.

[21]Nielsen, E. J. and Kleb, W. L., "Efficient Construction of Discrete Adjoint Operators on Unstructured Grids by Using Complex Variables," *43rd AIAA Aerospace Sciences Meeting and Exhibit*, Reno, NV, January 2005.

[22]Bil Kleb, R. A. T. and Johnston, C. O., "Blurring the Inputs: A Natural Language Approach to Sensitivity Analysis," *18th AIAA Computational Fluid Dynamics Conference*, Miami, FL, June 2007.

[23]Michele M. Putko, Arthur C. Taylor III, P. A. N. and Green, L. L., "Approach for Input Uncertainty Propagation and Robust Design in CFD Using Sensitivity Derivatives," *Journal of Fluids Engineering*, Vol. 124, No. 1, March 2002, pp. 60–69.

VII. Appendix

Table 5. Sensitivity of surface heating to reaction parameters compared with finite difference

Parameter	Parameter Value	Adjoint ($\frac{dL}{dD}$)	FD ($\varepsilon = D \times 10^{-3}$)	Fractional Sensitivity ($\frac{dL/L}{dD/D}$)
N2+O2 Dis	1.90E+017	7.27E-023	8.21E-023	3.17E-007
N2+NO Dis	1.90E+017	3.46E-022	3.58E-022	1.51E-006
N2+N Dis	4.09E+022	1.75E-026	1.98E-026	1.64E-005
N2+O Dis	1.90E+017	3.34E-021	3.41E-021	1.45E-005
N2+N2 Dis	4.70E+017	5.94E-021	6.04E-021	6.40E-005
O2+O2 Dis	3.24E+019	2.15E-022	2.16E-022	1.59E-004
O2+NO Dis	3.60E+018	6.41E-022	6.44E-022	5.29E-005
O2+N Dis	3.60E+018	4.36E-022	4.42E-022	3.60E-005
O2+O Dis	9.00E+019	4.27E-021	4.40E-021	8.82E-003
O2+N2 Dis	7.20E+018	8.07E-021	8.15E-021	1.33E-003
NO+O2 Dis	3.90E+020	6.36E-025	6.46E-025	5.68E-006
NO+NO Dis	7.80E+021	2.98E-024	2.99E-024	5.32E-004
NO+N Dis	7.80E+021	2.43E-024	2.49E-024	4.34E-004
NO+O Dis	7.80E+021	2.78E-023	2.87E-023	4.98E-003
NO+N2 Dis	3.90E+020	4.89E-023	4.95E-023	4.37E-004
NO formation (f)	7.00E+013	7.30E-015	7.63E-015	1.17E-002
NO breakdown (f)	3.20E+009	1.28E-010	1.32E-010	9.42E-003
N2+O2 Recom	1.10E+016	2.09E-023	4.64E-022	5.27E-009
N2+NO Recom	1.10E+016	9.04E-022	1.33E-021	2.28E-007
N2+N Recom	2.27E+021	5.01E-024	4.98E-024	2.60E-004
N2+O Recom	1.10E+016	1.20E-019	1.20E-019	3.04E-005
N2+N2 Recom	2.72E+016	1.83E-019	1.82E-019	1.14E-004
O2+O2 Recom	2.70E+016	2.89E-018	2.89E-018	1.79E-003
O2+NO Recom	3.00E+015	5.99E-019	6.01E-019	4.12E-005
O2+N Recom	3.00E+015	7.80E-019	7.79E-019	5.36E-005
O2+O Recom	7.50E+016	1.93E-017	1.93E-017	3.32E-002
O2+N2 Recom	6.00E+015	4.06E-017	4.06E-017	5.58E-003
NO+O2 Recom	1.00E+020	1.59E-025	2.18E-025	3.65E-007
NO+NO Recom	2.00E+021	1.15E-024	1.13E-024	5.26E-005
NO+N Recom	2.00E+021	2.69E-023	2.68E-023	1.23E-003
NO+O Recom	2.00E+021	1.86E-022	1.87E-022	8.53E-003
NO+N2 Recom	1.00E+020	2.87E-022	2.86E-022	6.58E-004
NO formation (b)	1.56E+013	-3.22E-014	-3.13E-014	-1.15E-002
NO breakdown (b)	1.30E+010	-2.96E-011	-2.93E-011	-8.83E-003

Table 6. Sensitivity of surface heating to energy coupling parameters compared with finite difference

Parameter	Parameter Value	Adjoint ($\frac{dL}{dD}$)	FD ($\varepsilon = D \times 10^{-3}$)	Fractional Sensitivity ($\frac{dL/L}{dD/D}$)
O2 T-Tv coupling fit	1.29E+002	-3.31E-005	-2.75E-005	-9.80E-005
NO T-Tv coupling fit	1.68E+002	-4.32E-005	-3.76E-005	-1.66E-004
N2 T-Tv coupling fit	2.20E+002	-3.55E-003	-3.55E-003	-1.79E-002

Table 7. Sensitivity of surface heating to transport parameters compared with finite difference

Parameter	Parameter Value	Adjoint ($\frac{dL}{dD}$)	FD ($\varepsilon = D \times 10^{-3}$)	Fractional Sensitivity ($\frac{dL/L}{dD/D}$)
O2 Transport-1	4.49E-002	7.72E+001	7.69E+001	7.95E-002
O2 Transport-2	-8.26E-002	1.06E+001	1.06E+001	-2.00E-002
O2 Transport-3	-9.20E+000	1.45E+000	1.45E+000	-3.06E-001
NO Transport-1	4.36E-002	1.35E+001	1.34E+001	1.35E-002
NO Transport-2	-3.36E-002	1.76E+000	1.76E+000	-1.36E-003
NO Transport-3	-9.58E+000	2.31E-001	2.31E-001	-5.06E-002
N Transport-1	1.16E-002	1.22E+001	1.21E+001	3.24E-003
N Transport-2	6.03E-001	1.46E+000	1.46E+000	2.02E-002
N Transport-3	-1.24E+001	1.75E-001	1.75E-001	-4.99E-002
O Transport-1	2.03E-002	2.94E+002	2.94E+002	1.37E-001
O Transport-2	4.29E-001	3.69E+001	3.69E+001	3.63E-001
O Transport-3	-1.16E+001	4.64E+000	4.64E+000	-1.23E+000
N2 Transport-1	2.68E-002	9.26E+002	9.34E+002	5.69E-001
N2 Transport-2	3.18E-001	1.19E+002	1.19E+002	8.68E-001
N2 Transport-3	-1.13E+001	1.54E+001	1.54E+001	-4.00E+000